Journal of Naval Architecture and Marine Engineering
January, 2026
https://doi.org/10.3329/jname.v23i1.79105 http://www.banglajol.info

HYDRODYNAMIC FORCES AND MOMENTS ON UNDERWATER VEHICLES: A NUMERICAL INVESTIGATION USING FLOW AND BODY ROTATION AT VARIOUS ANGLES OF ATTACK

H. Rahul Krishna[1*], M. T. Issac[2] and D. D. Ebenezer[3]
Department of Ship Technology, Cochin University of Science and Technology (CUSAT), Kochi, Kerala, India- 682022, Email:[1*]r4rahul4k@yahoo.co.in, [2]m.issac@cusat.ac.in, [3]d.d.ebenezer@gmail.com

Abstract:

Accurate numerical simulation of flow over bodies, when there is an angle of attack, is challenging even when the body is slender and axisymmetric. Two methods are widely used in such simulations, but no study clearly compares the accuracies and the advantages and disadvantages of the methods. In the body rotation method (BRM), the flow is along the axis of the domain, and the body is rotated such that the angle between the main axis of the body and the flow direction is the angle of attack. In the flow rotation method (FRM), the axis of the body is along the axis of the domain, and the direction of the flow is changed to simulate the angle of attack. In the present study, both methods are used at a Reynolds number of 12×10^6. *The Computational Fluid Dynamics (CFD) package is used to simulate flow over an axisymmetric three-dimensional (3D) bare hull submarine model, and the angle of attack is varied from 0° to 18°. In both BRM and FRM approaches, steady Reynolds Average Navier Stokes (RANS) equations are solved using the* $k-\omega$ *Shear Stress Transport (SST) turbulence model, with non-dimensional wall adjacent cell thickness* (Y_w^+) *kept below 1. The same domain and mesh commands are used in both methods. The hydrodynamic forces, moments, coefficients of wall shear stress, and pressure computed using the two methods differ by less than two percent. The distribution of the sizes of cells and the number of cells of various shapes are also presented. When meshed with cells in the wall-adjacent region having the same size, the number of cells and computation time are much less in the body rotation method, and it is therefore preferred.*

Keywords: Angle of attack, axisymmetric bodies, CFD, DARPA SUBOFF, non-axisymmetric flows, RANS modeling.

1. Introduction

Analysis of turbulent axial flow over axisymmetric bodies using two-dimensional (2D) axisymmetric Computational Fluid Dynamics (CFD) simulations provides quick results that are approximately equal to those obtained using three-dimensional (3D) simulations but with significant savings in computational time and resources (Krishna et al., 2023). However, the 2D approach is not useful for modeling turbulent flow at various angles of attack, even over axisymmetric bodies, as even the mean flows are inherently three-dimensional. For Angle of Attack (AoA) simulations, two methods are in use. The body is rotated in the Body Rotation Method (BRM), and the flow is aligned with the horizontal axis of the domain. For each angle of attack simulation, the body is rotated to the corresponding AoA. For each angle, a new mesh and boundary conditions, and perhaps a new domain are needed. The flow is rotated in the Flow Rotation Method (FRM), and the body remains aligned with the horizontal axis of the domain. Several authors report studies using one of the two methods. However, a direct comparison of the effort needed to execute these methods and the results obtained using them has not been done. In this paper, flows over the bare hull axisymmetric of the Defence Advance Research Project Agency Submarine model (DARPA SUBOFF) at various angles of attack is studied using both methods to decide which is more effective. The bare hull used in this study is the Anechoic Flow Facility (AFF -1) hull form mentioned in Liu and Huang (1998). The hydrodynamic forces and moments are also computed by meshing the full (360° bodies of revolution) and half bodies (180° bodies of revolution) to appreciate the effects of assuming a symmetry plane. A detailed literature review of numerical works done using either method is presented first.

The Body Rotation Method is used by many for AoA studies. Sakthivel et al. (2011) used this method on a bare hull configuration of the MAYA Autonomous Underwater Vehicle (AUV) using a cylindrical domain, and the flow was along the axis of the domain at a Reynolds number (Re) of 2.09×10^6. The maximum angle of attack was 20°. The study also highlighted the significance of circumferential pressure gradients in flow variables at

1813-8535 (Print), 2070-8998 (Online) *Received: Jan., 2025*

higher angles of attack. Gomatam et al. (2012) used the BRM for a cuboidal domain to study the MAYA AUV with control surfaces at AoA varying from -20° to +20°. Gross et al. (2013) used the BRM in direct numerical simulations (DNS) to study unsteady three-dimensional flow over axisymmetric bodies at large angles of attack and compared their results with those obtained using a water tunnel. Shereena et al. (2013) used the BRM approach with a cylindrical domain to study the effect of injecting air jets in the boundary layer region on the drag of an axisymmetric bare hull body. AoA of 0°, 5°, and 15° were considered. Leong et al. (2015) used a cuboidal domain and the BRM for numerically simulating the bare hull DARPA SUBOFF submarine model at various drift angles ranging from 0° to +18°. Ray et al. (2016) used the BRM to study unsteady flow over the AUV-150 and estimate hydrodynamic forces and moments up to 20° angles of attack using a cylindrical domain. Mohamed et al. (2017) used the BRM to study the effect of AoA, strut position, and free surface in determining the hydrodynamic forces and moments for an axisymmetric body. A cubical domain was used and the results were in good agreement with experimental values up to 15° AoA. Madan and Issac (2017) used the BRM to study the effect of varying the slenderness ratio (Length to diameter ratio – *l/d*) of an AUV on the hydrodynamic forces and moments for angles of attack up to 20°. A 3D model with a 360° body of revolution in a cuboidal domain was used for the numerical simulations. Takahashi and Sahoo (2019) utilized the BRM on the 3D bare hull configuration of DARPA SUBOFF with a 360° body of revolution with a cuboidal domain for simulating the angle of attack cases up to 18°. Ray et al. (2009) have used the BRM method to determine non-dimensional sway force and yaw moment at various angles of attack (transverse velocity) for the bare hull DARPA SUBOFF model. Later, they used these results to estimate linear and non-linear hydrodynamic coefficients of DARPA SUBOFF. Kumar et al. (2023) used BRM to study the pressure, velocity, turbulence, wall shear stress behavior, hydrodynamic forces, and moments on an appended Autonomous Underwater Vehicle at angles of attack ranging from 0° to 10°. Le and Hong (2021) applied this BRM method on a torpedo-shaped underwater glider to study the hydrodynamic characteristics like drag and lift forces acting on the vehicle at varying angles of attack (2°, 10°, and 30°) at glider speeds ranging from 0.9 – 1.1 m/s. Comsol Multiphysics software was used to carry out the numerical analysis in their study. The BRM method is also used for non-axisymmetric bodies. Ebrahimnejad et al. (2014) used the BRM for non-axisymmetric bodies, which are blunt, to estimate aerodynamic coefficients for the angle of attacks up to 15° using unsteady simulations. Subburaj et al. (2018) used the BRM to study flow over an elliptical cylinder near a free surface at a very low *Re* and investigated the effect of AoA (-45°, +45°, and +90°), aspect ratio, submergence depth, and Froude number on the flow. Lin et al. (2024) used BRM to investigate the hydrodynamic performance of a finite-length rotating column with two free ends at various angles of attack using Large Eddy Simulation (LES).

The FRM is used by a few to study bare hull axisymmetric bodies. de Baross et al. (2008) used a 180° model to analyze flow over the MAYA AUV to estimate hydrodynamic forces and moments up to 25° angle of attack. Gross et al. (2011) used a 180° model of the DARPA SUBOFF to investigate the coefficient of pressure and wall shear stress, velocity, and eddy viscosity distribution at 18° angle of attack using the FRM method. Praveen and Krishnankutty (2013) studied the effect of AUV body length up to a 10° angle of attack, and the results were compared with solutions from Semi-Empirical (SE) methods. Ray (2010) has used both the BRM and FRM methods for oblique tests on appended DARPA SUBOFF. He used BRM for determining hydrodynamic forces and moments in the horizontal plane and FRM for determining these forces and moments in the vertical plane. A direct comparison of BRM and FRM results was not done in this paper. Even though the FRM requires less human time and effort than the BRM, it is used less often.

Several authors have reported studies utilizing either the BRM or the FRM. However, a direct comparison of the computational effort required and the results produced by these two methods has not been previously undertaken. This study addresses that gap, presenting a novel comparison between BRM and FRM. Additionally, the research highlights the limitations of using a symmetry plane, specifically the emergence of scallops in the coefficient of pressure and shear stress distributions. These insights are expected to guide future research on underwater vehicles by helping researchers select the most suitable CFD method and apply it more effectively.

In the present paper, the benchmark underwater vehicle, the Defence Advance Research Project Agency Submarine model (DARPA SUBOFF) with an axisymmetric bare hull is used. A rigorous comparison of the mesh and the results obtained using the two methods is presented for the Angle of Attack up to 18°. It is shown that there exist small differences between the drag, lift, coefficient of pressure, coefficient of wall shear stress, and velocity field obtained using the BRM and the FRM methods. However, a detailed cell volume analysis reveals that, for the same large domain and at the highest AoA, the FRM requires significantly more cells in mesh than

the BRM. The effect of using a symmetry plane in a 180° model is also studied. The studies are used to show that it is more suitable to use the BRM.

The sections in this paper are organized as follows. In Section 2, the methodology adopted for implementing the 3D numerical simulations using BRM and FRM methods is described. In Section 3, the convergence, uncertainty, discretization error, and Richardson Extrapolation are presented. In Section 4, the numerical results from the BRM and FRM methods are presented. A rigorous comparison is done on the hydrodynamic forces and moments, the coefficient of pressure and wall shear stress, and the velocity profiles obtained using the two methods. Verification and validation are done at three levels. The conclusions are in Section 5.

2. Geometry and Computational Details

2.1 The DARPA SUBOFF

The bare-hull benchmark DARPA SUBOFF submarine model is a streamlined axisymmetric body with an overall length of 4.356 m and a maximum diameter of 0.508 m (Groves et al., 1989), as shown in Fig. 1.

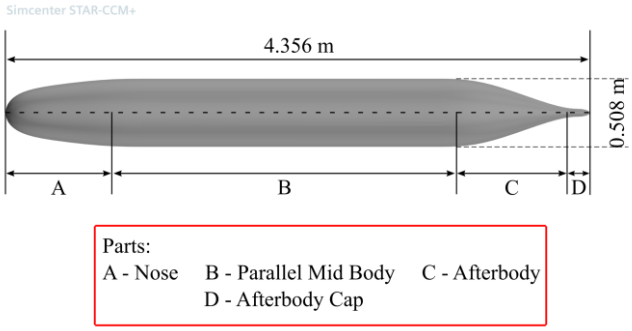

Fig. 1: The axisymmetric benchmark DARPA SUBOFF with overall length, l = 4.356 m and diameter, d = 0.508 m (Krishna et al., 2023).

2.2 The flow rotation and body rotation methods

The 360° and 180° bodies of revolution models are used in the FRM. Only the 360° model is used in the BRM, and the body is rotated about the center of volume located at 2.013 m aft of the nose along the body axis. Rotation is in the horizontal x-y plane, by an angle of attack, α, as shown in Fig. 2. The flow is along the x-axis of the domain. In the FRM, the flow is rotated and makes an angle α with the x-axis as shown in Fig. 2. The hydrodynamic forces and moments are numerically computed about the center of volume, as the David Taylor Research Center (DTRC) experimental measurements of these forces and moments are done at this point (Roddy, 1990). In Fig. 2, the blue coordinate system is aligned along the flow direction. It is used to find the Lift (L) and Drag (D) forces. The red coordinate system is oriented along the axis of the body. It is used to find the Axial (X) and Normal (Y) forces.

2.3 The computational domain

The same computational cuboidal domain is used for the BRM and the FRM, as shown in Fig. 2. The inlet is $10\,l$ upstream of the nose, where l is the length of the DARPA SUBOFF. For the 360° models, the transverse cross-section of the domain is a square whose boundaries are at $6l$ from the axis of the body before rotation. In 180° models, a symmetry plane that cuts the body in half and forms one face of the boundary of the domain is used. In the transverse cross-section, one edge lies on this plane and is $12\,l$ long and three planes are at $6l$ from the axis of the body. The outlet is at $20\,l$ from the tail of the body. Therefore, the total length of the domain is $31\,l$ for all the cases. These dimensions for the domain are recommended by the ITTC (2014) for non-zero angle of attack studies.

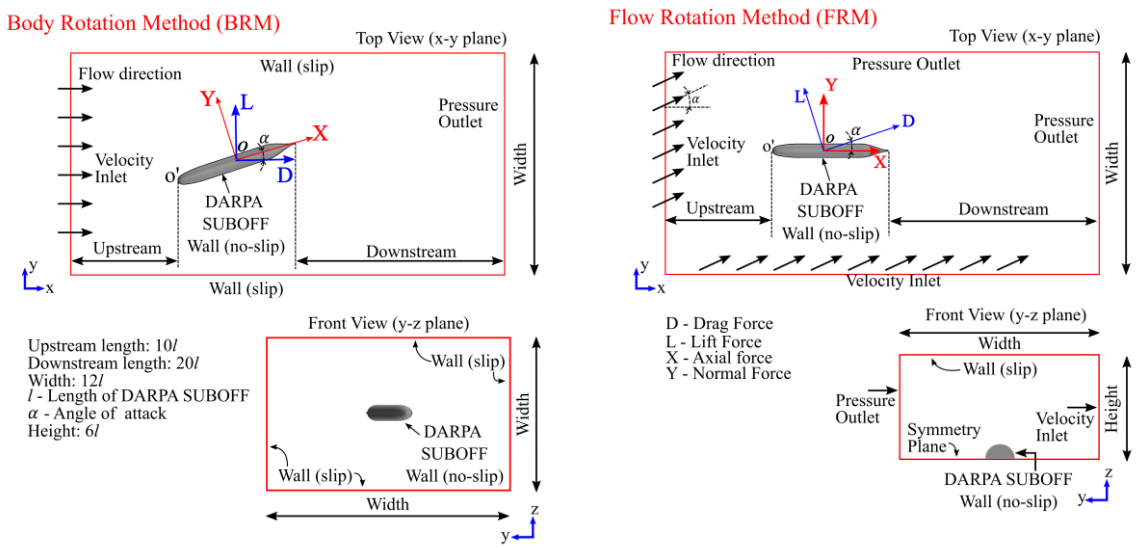

Fig. 2: The top-view (*x*-*y* plane) of the domain and the boundary conditions for the Body Rotation Method and the Flow Rotation Method. A transverse cross-section for a 180° model is also shown.

2.4 Boundary conditions and physics models

The boundary conditions used in the BRM and the FRM are shown in Fig. 2. The flow is from left to right in the BRM. On the left face of the domain, inlet conditions are specified, and the specified velocity is uniform. On the right face of the domain, pressure outlet conditions are specified. Slip-wall conditions are specified on the four other faces of the domain. For the FRM, the flow is rotated in the horizontal plane at the inlet. The top and bottom faces of the domain are slip-walls for a 360° model of DARPA SUBOFF, whereas the bottom face is a symmetry plane for a 180° model of DARPA SUBOFF. The left and front faces are inlets, and the flow angle is specified by prescribing the three components of uniform inlet velocity on these faces. The z component of the velocity is zero on both faces. Pressure outlet conditions are prescribed on the right and back faces. In both BRM and FRM, the surface of the DARPA SUBOFF is treated as a wall under no-slip condition.

In the BRM and FRM approaches, the steady Reynolds Averaged Navier Stokes (RANS) equations are solved to determine various flow parameters, including hydrodynamic forces, moments, pressure, velocity, and wall shear stress distributions. The RANS model utilizes six Reynolds stresses, defined as functions of eddy viscosity, to describe the flow. In STAR-CCM+™, the finite volume method (FVM) is used. The primary variables solved in each cell are pressure and velocity, employing the semi-implicit method for pressure-linked equations, commonly known as the SIMPLE algorithm. The solution approach is segregated, addressing pressure and velocity sequentially in RANS. The closure of the RANS model involves employing a two-equation eddy viscosity model known as $k-\omega$ with a shear stress transport (SST) variant. This turbulence model resolves turbulent kinetic energy (k) and specific dissipation rate (ω). The choice of this particular turbulence model is motivated by its enhanced performance in the boundary layer region, particularly under adverse pressure gradients. Additionally, the model is effective for very low values of the normalized thickness of the wall-adjacent cells (Y_w^+) treatments. Default values for turbulent intensity and turbulent viscosity ratio in STAR-CCM+ ™ for BRM and FRM are set at 0.01 and 10, respectively. The fluid is incompressible water at 15℃ with density, ρ = 999.1026 kg/m^3 and viscosity, μ =1.14× 10^{-3} Pa.s (ITTC, 2011).

2.5 Mesh

The same procedure for meshing is used in the BRM and the FRM. The meshes are shown in Fig. 3. A background mesh is generated with a target size of 0.4 m and a maximum size of 2 m. It is predominantly hexahedral in nature. ITTC has recommended a domain size, but has not recommended the size of the largest cell in the domain. The surface of the DARPA SUBOFF is refined using custom-type refinement. The target size for cell edge lengths is 6 mm in the nose and tail regions and 9 mm in the mid-body region. The x coordinates used to generate the geometry of the body have a uniform spacing of 3 mm. This is one-half of the target edge lengths in the nose and

tail regions and one-third of the target edge length in the mid-body region. Such a fine geometry definition is necessary to obtain accurate results.

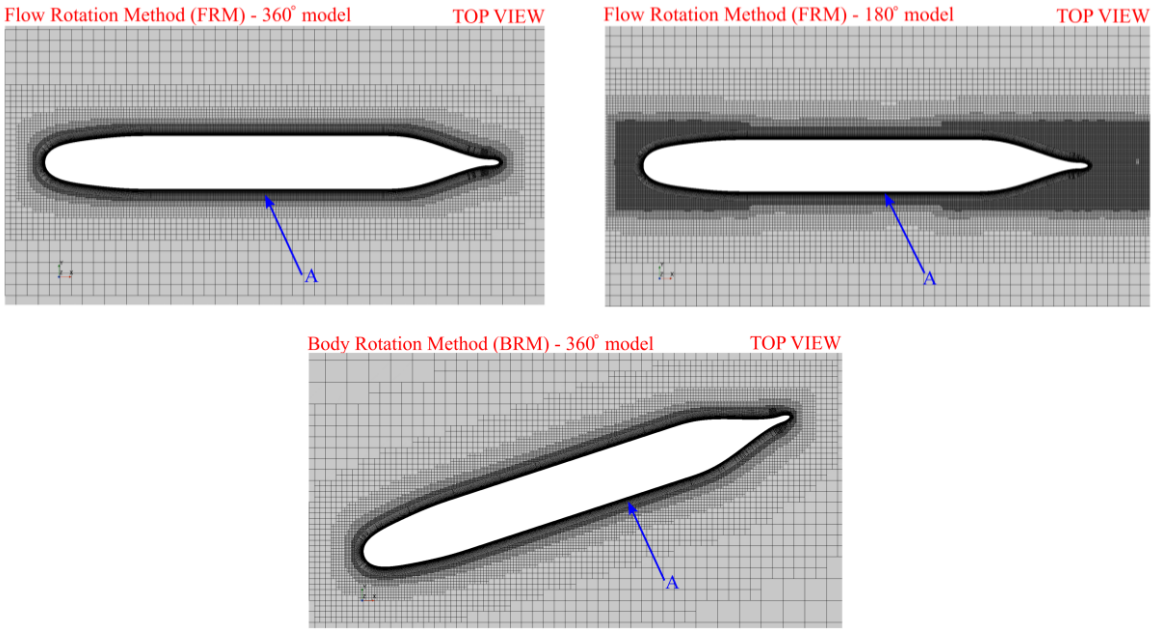

Fig. 3: Sectional top view of mesh used in the BRM and the FRM approaches. The arrow (A) points to the very fine prism layer mesh.

Prism layers that envelope the body are used to mesh the boundary layer region. The wall-adjacent prism layer is very thin in the direction normal to the wall and inherits its lateral dimensions from the surface refinement. Thus, it has a high aspect ratio. The thicknesses of the prism layers form a geometric progression. The thickness of the wall-adjacent layer is a, the growth factor is r, and the total number of layers is N_p. The initial values of these parameters are estimated and then refined. As the $k-\omega$ SST turbulence model is used, the normalized thickness of all the wall-adjacent cells, $Y_w^+ = y_p \frac{u_\tau}{v}$ should be less than 1, where $y_p = a/2$ is the distance between the wall and the centroid of the wall-adjacent cell, v is the kinematic viscosity, $u_\tau = \sqrt{\frac{\tau_w}{\rho}}$ is the frictional velocity, τ_w is the wall shear stress, and ρ is the density. The normalized thickness depends on the local wall shear stress. Therefore, a small value of a is used to run the job and Y_w^+ is computed for all the wall-adjacent cells. Then, a revised value of a is used to generate the mesh. In the final mesh, a = 7.26 micron. The total thickness of the prism layers is $S_N = a(r^{N_p} - 1)/(r - 1)$. This total thickness should be more than the thickness of the region within which there are large gradients in the flow, but it is not easy to estimate this thickness. Therefore, one option is to estimate the thickness by using the expression for the boundary layer thickness of a flat plate with a length equal to that of the DARPA SUBOFF. Then, the mesh is generated and the simulation is executed. Then the velocity contour map is inspected, a revised estimate of the thickness is made, and a new mesh is generated. In the final mesh, r = 1.11, N_p= 68 and $S_N \cong$ 79.6 mm. The last cell in the prism layer has a thickness of $b = ar^{N_p - 1} \cong$ 7.9 mm, which helps in maintaining a good aspect ratio outside the prism layer region. Volume refinement with a target size of 7.5 mm is done in two cylinders whose dimensions are chosen to ensure that the flow around the body is captured well. The cylinders are co-axial with the body, and the radius of both cylinders is 0.4 m. The target size in the entire domain is 400 mm and the maximum cell size is 2,000 mm. Therefore, to transition from the cells with a 7.5 mm edge length within the two cylinders and a 9 mm edge length in the mid-body region between them, to the outer region with 400 mm, STAR-CCM+™ uses several intermediate sizes. Cells with edge lengths of 13.3, 26.6, 53.2, 106, 213, 426, 852, and 1,704 mm are generated in both BRM and FRM. Hanging nodes are used for the transition from one edge length to the next, and the cell edge length doubles at every transition step. In the FRM, the mesh is generated such that it is sufficiently fine in a large volume for the highest angle of attack, α, of 18.11°, which results in the most complex flow, and the same mesh is used for all the angles of attack. The meshes used in BRM and FRM are shown in Fig. 3. The mesh type for BRM and FRM approach is 3D unstructured automated trimmed

cells with prism layers. Trimmed cells are predominantly hexahedral type and are high-quality cells with low skewness. The meshes in BRM and FRM have a Y_w^+ value less than 1 with a max value of 0.72 in both methods.

2.6 Cell count

The total number of cells in a mesh is very important. Higher accuracy often comes at higher computational costs. However, higher computational costs need not lead to higher accuracy. The total number of cells in the BRM 360°, FRM 360°, and FRM 180° models are 24.43 M, 34.51 M, and 18.85 M, respectively, at AoA = 18.11°. Notably, the FRM 360° mesh has 41% more total cells than the BRM mesh. The details regarding the distribution of the sizes of cells and the number of cells of various shapes are presented in Tables 1 and 2.

The domain size remains the same in both BRM-360° and FRM-360° models and is not the reason for a low mesh count in BRM-360° compared to FRM – 360°. The FRM-360° mesh has 66% more hexahedral cells (31.50 M) than the BRM mesh (18.97 M). The difference in the number of hex cells, 12.53 M, is the primary reason for the extra 10.08 M of total number of cells that the FRM 360° mesh has compared to the BRM mesh (refer to Table 1). The number of cells whose volumes are between several sets of upper and lower thresholds is shown in Table 2. As explained in the previous section, there are several cubical hexahedral cells. They have edge lengths of 13.3, 26.6, 53.2, … 1,704 mm as shown in column 1 of Table 2. The volumes are cubes of these edge lengths and are shown in column 2 of Table 2. A very small number of cells outside the prism layers are not cubical, as volume refinement is done inside cylinders, and the domain is cuboidal. As there may be a few slightly large cells, the thresholds for the volumes are set at 1% more than the volumes in column 3. The lower and upper bounds for several volume bands are shown in column 4. The number of cells in these bands is shown in columns 5 and 6 for the BRM and FRM (360°) meshes, respectively. The number of cells with volumes in the range of 1.52×10^{-4} to 1.22×10^{-3} m^3 is 1.99 M in FRM and 0.11 M in BRM, with volumes in the range 1.22×10^{-3} to 9.76×10^{-3}m^3 is 9.08 M in FRM and 1.44 M in BRM, and with volumes in the range of 9.76×10^{-3} to 0.078 m^3 is 6.26 M in FRM and 4.53 M in BRM as shown in rows 3, 4, and 5 of Table 2. This accounts for the additional 10.08 M of cells present in FRM compared to BRM. It is seen from Fig. 3 that the larger cells are near the corners of the cuboids. For a lesser AoA than 18.11°, the difference in the number of cells between BRM and FRM is less. For zero AoA, the meshes are identical. In the longitudinal sections in Fig. 3, it is seen that in the BRM mesh, within the rectangular region shown, the top left and bottom right corners have a low-density mesh. However, in the FRM 360 deg mesh, the entire rectangle has cells of the same size. Having a slightly greater number of cells in the prism layer region of BRM compared to FRM provides an additional benefit for accurately capturing the turbulent boundary layer.

Table 1: Number and types of cells in various regions in BRM and FRM meshes

Parameter	**BRM - 360**	**FRM - 180**	**FRM - 360**
Cell Type			
Hexahedral cells	(18.97 M)	(17.37 M)	(31.50 M)
Wedge cells	(4.82 M)	(0.89 M)	(1.86 M)
Polyhedral cells	(0.61 M)	(0.56 M)	(1.13 M)
Tetrahedral cells	(0.034 M)	(0.006 M)	(0.01 M)
Cell Distribution			
Prism Layer region	(15.19 M)	(7.08 M)	(14.36 M)
Region between domain Boundaries and last prism layer	(8.12 M)	(10.48 M)	(17.23 M)
Domain Boundaries (Inlet, Outlet, surrounding Wall/symmetry plane)	(1.12 M)	(1.73 M)	(2.92 M)
Total Cell Count	**24.43 million**	**18.85 million**	**34.51 million**

3. Grid Sensitivity Analysis – Richardson Extrapolation

To quantify the uncertainty linked to the finest mesh, Richardson Extrapolation (RE) is used. RE allows the assessment of how closely the results obtained using the finest mesh agree with those derived from an ideal mesh.

In the present study, highly refined mesh cells are used in the prism layer region, and the fine mesh has a maximum value of Y_w^+ less than unity. Three different representative cell sizes (h_i) are selected here for RE study, and the corresponding CFD solutions for axial force, normal force, and moment are φ_i where $i = 1, 2,$ and 3 represent fine, medium, and coarse meshes, respectively. The wall adjacent layer thickness, a_i, is chosen as the representative cell size ($h_i = a_i$). The values of a_1, a_2, and a_3 are 7.260, 10.267, and 14.519 microns, respectively.

Table 2: Number of cells in BRM and FRM

Nominal cell edge length (m) (1)	Nominal cell volume (m^3) (2)	Volume Threshold – 1% more than nominal cell volume (m^3) (3)	Volume Threshold (m^3) (4)	Cell count (Millions) in each region of threshold volume in BRM – 360 (5)	Cell count (Millions) between each region of threshold volume in FRM – 360 (6)
1.7040	4.95	4.99	0.625 – 4.99	0.17	0.38
0.8520	0.619	0.625	0.078 – 0.625	0.61	0.27
0.4260	0.077	0.078	9.76×10^{-3} – 0.078	4.53	6.26
0.2130	9.66×10^{-3}	9.76×10^{-3}	1.22×10^{-3} - 9.76×10^{-3}	1.44	9.08
0.1064	1.21×10^{-3}	1.22×10^{-3}	1.525×10^{-4} - 1.22×10^{-3}	0.11	1.99
0.0532	1.51×10^{-4}	1.525×10^{-4}	1.898×10^{-5} - 1.525×10^{-4}	0.13	0.12
0.0266	1.88×10^{-5}	1.898×10^{-5}	2.37×10^{-6} - 1.898×10^{-5}	0.4	0.35
0.0133	2.35×10^{-6}	2.37×10^{-6}	PL - 2.37×10^{-6}	1.84	1.69
			Prismatic region (PL region)	15.19	14.36
			Total cell count	**24.43**	**34.51**

The representative cell size is selected based on the guidelines (Celik et al. 2008 and Krishna et al, 2023). The value of a_1 is chosen such that Y_w^+ is less than 0.5. Then, the values of a_2 and a_3 are selected such that the refinement factor ($\gamma_{i+1,i} = a_{i+1}/a_i$) $\cong 1.414$. The growth rate, r, is nearly 1.11. The value of N_{p_i} is estimated for constant values of $S_{N_i} = 0.09$ and $r \cong 1.11$. The values of N_i for the fine, medium, and coarse meshes are 68, 66, and 63, respectively. The last cell thickness in the prism layer is $\cong$ 9 mm for all the cases. As a result, the ratio of the volumes of cells just inside and outside the prism layers is satisfactory.

The RE method is used to determine the ideal solution, φ_0, when h_i tends to zero. φ_0 is calculated using $\varphi_0 = \frac{\gamma_{21}^P \varphi_1 - \varphi_2}{\gamma_{21}^P - 1}$. Here, $P = \frac{1}{\ln(\gamma_{21})}\left[\ln|\varepsilon_{32}/\varepsilon_{21}| + \ln\left(\frac{\gamma_{21}^P - S}{\gamma_{32}^P - S}\right)\right]$ is the order of accuracy and $S = sign(R)$, where $R = \varepsilon_{32}/\varepsilon_{21}$ and $\varepsilon_{i+1,i} = \varphi_{i+1} - \varphi_i$. The convergence is monotonic if $0 < R \leq 1$, oscillatory if $-1 \leq R < 0$, and diverges if $|R| > 1$. The uncertainty associated with the fine mesh used here is defined using the Grid Convergence Index, $GCI_{21} = \frac{f_s e_{21}}{\gamma_{21}^P - 1}$ where f_s is the factor of safety taken as 1.25 (ITTC, 2021), and $e_{21} = |(\varphi_2 - \varphi_1)/\varphi_1|$ is the relative error between fine and medium mesh.

4. Numerical Results

Verification and Validation (V&V) are done at three levels. At the first level, are the quantities that are integrals: the drag, the lift, and the hydrodynamic moment on the DARPA SUBOFF computed using the BRM 360°, FRM 360°, and FRM 180° models as a function of angle of attack. At the second level are functions that vary over the surface of the body: the coefficient of pressure and the wall shear stress. The velocity field is at the third level as it is function of space. Results are presented at angles of attack, α, ranging from 0 to 18.11°. The values of α are the same as those in the DTRC literature (Roddy 1990).

4.1 Y_w^+ - Normalized thickness of the wall-adjacent cells

For the finest mesh, $Y_w^+ < 1$ everywhere. It is higher in the regions where the velocity near the body is higher. The maximum value of Y_w^+ for the finest mesh is about 0.72 as shown in Fig. 4, whereas the maximum values for the medium and coarse meshes are 1.02 and 1.44, respectively.

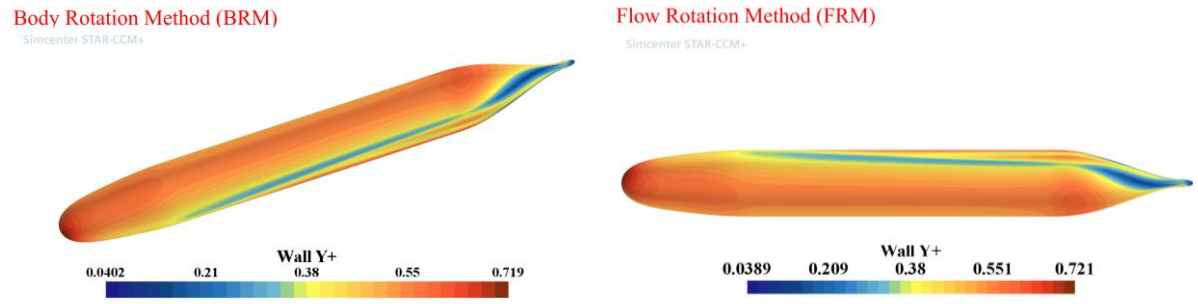

Fig. 4: Distribution of Y_w^+ on the surface of DARPA SUBOFF in BRM and FRM (top view) when $\alpha = 18.11°$ and the finest mesh is used (a = 7.260 microns).

4.2 Hydrodynamic forces and moments

The hydrodynamic forces and moments determined are shown in Fig. 5 for various angles of attack. The axial, normal, and moment coefficients are $X' = X/(0.5\rho u^2 L_{pp}^2)$, $Y' = Y/(0.5\rho u^2 L_{pp}^2)$, and $N' = N/(0.5\rho u^2 L_{pp}^3)$, respectively, where X and Y are the axial and normal forces along the body nose-tail direction and normal to it, respectively, and N is the moment about the center of volume and the length between perpendiculars, L_{pp} = 4.261 m. The forces and moments are first determined for the speed, u = 3.34 m/s, at which experimental results are available and the highest angle of attack is 18.11°. The results, $\varphi_i, i = 1, 2, 3$, are shown in Table 3.

Table 3: Grid sensitivity analysis using Richardson Extrapolation

Parameter	**Values**		
a_1, a_2 *and* $a_3(\mu m)$	7.260, 10.267 and 14.519		
Total number of cells (in millions)	24.43 M, 24.22 M and 23.91 M		
Max (y_w^+)	0.72, 1.02 and 1.44		
N_{p_1}, N_{p_2} *and* N_{p_3}	68, 66 and 63		
r	1.11		
γ_{21}, γ_{32}	1.414, 1.414		
Solution	Axial Force (N)	Normal Force (N)	Moment (Nm)
φ_1	72.80	611.864	1443.93
φ_2	71.99	609.682	1445.30
φ_3	70.61	606.020	1447.52
φ_0	73.95	615.080	1441.72
Exp Value	67.90	745.860	1290.21
(% Difference between Exp value and φ_0*)*	(-0.1%)	(17.5%)	(-11.7%)
ε_{21} ε_{32}	-0.81 -1.38	-2.182 -3.662	1.37 2.22
R	0.587 (Monotonic Convergence)	0.596 (Monotonic Convergence)	0.617 (Monotonic Convergence)
P (Order of accuracy)	1.54	1.50	1.39
e_{21}	1.11%	0.36%	-0.10%
e_e	1.56%	0.52%	-0.15%
$\boldsymbol{GCI_{21}}$	**2.0%**	**0.66%**	**-0.19%**

All iterations are done until five significant digits of the normal force converge and do not change for 1,000 iterations. The axial force computed using the finest mesh is 3% greater than that computed using the coarsest mesh. This occurs even when the max (Y_w^+) for the finest and coarsest are 0.72 and 1.44, respectively. The difference is considerable and illustrates the importance of using a fine mesh. Richardson Extrapolation is used to

find the forces and moment, φ_0, when the mesh size is zero. The values of hydrodynamic forces (especially drag, lift, axial and normal forces) and moments are monitored after every 500 iterations. The convergence is obtained in 6,500 iterations. The residual values for continuity, momentum, specific dissipation rate and turbulent kinetic energy are lowered below 1×10^{-6} for FRM, whereas it is below 1×10^{-5} for the BRM approach.

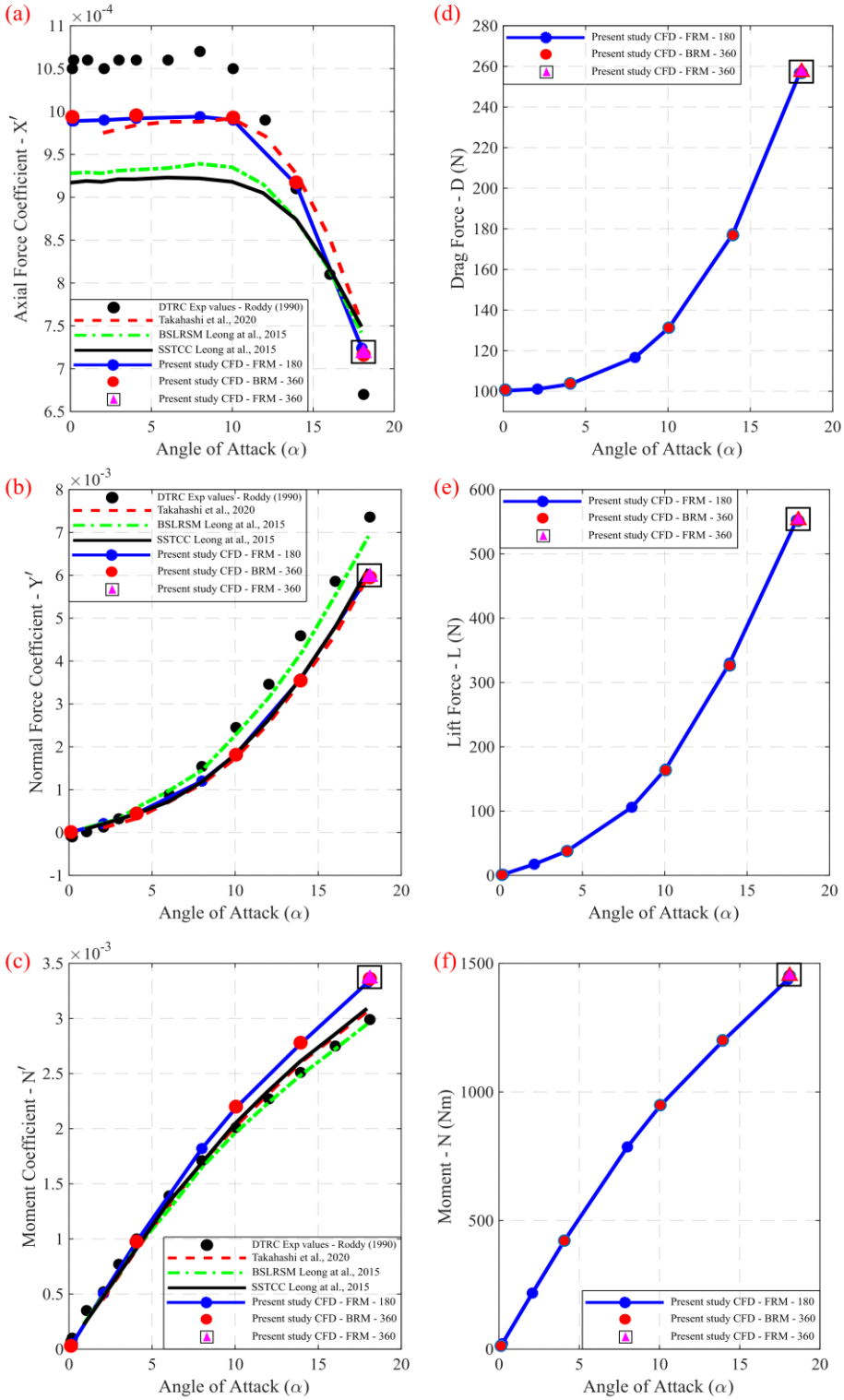

Fig. 5: (a) Axial (b) normal (c) moment coefficients (e) drag (d) lift and (f) moment at various angles of attack.

In Fig. 5, the forces and moment computed at $Re = 12.5\times \mathbf{10^6}$ ($\boldsymbol{u = 3.34}$ m/s) using BRM and FRM are compared with the experimental results of Roddy (1990) which are at about $Re = 14\times \mathbf{10^6}$ and the CFD results of Takahashi and Sahoo (2019) and Leong et al., (2015) which are at $Re = 14\times \mathbf{10^6}$. Roddy presents results at the same velocity but the *Re* is about $14\times \mathbf{10^6}$. He notes "These experiments indicate that the non-dimensional hydrodynamic force and moment coefficients vary with Reynolds number up to a Reynolds number based on the length of the hull of about 10 to 15 million, but above this value the coefficients no longer significantly change with Reynolds number." Therefore, the comparison of results at various *Re* between 12.5 and 14.2 million is reasonable.

At the highest AoA, α =18.11°, the maximum difference between the axial, normal, and moment coefficients computed using the BRM 360°, FRM 360°, and FRM 180° model is less than 1%. Therefore, the internal consistency in the results is good. The normal force computed here is in very good agreement with those obtained by Takahashi and Sahoo (2019) over the entire range of AoA. The axial force and the moment are also in good agreement. When all the CFD and experimental results are considered, it is seen from Fig. 5a that as the Ao A increases, the axial force coefficient and the spread in it decrease. At each AoA, the present axial forces are approximately the mean of all the forces. As the AoA increases, the normal force coefficient in Fig. 5b starts at zero but becomes about 10 times the axial force coefficient at AoA = 18.11°. The normal force coefficient computed here is in good agreement with those obtained by Takahashi and Sahoo (2019) and by Leong et al.(2015). The experimental results of Roddy (1990) and the results of Leong et al.(2015) are a little higher. The moment coefficient is shown in Fig. 5c. All the results are nearly the same for AoA< 5°. At higher AoA, the spread increases. At AoA = 18.11°, the present results are about 10% more than the other results. The hydrodynamic forces like drag and lift, and moments are shown in Fig. 5d to 5f. At AoA = 18.11°, the drag is about 2.5 times the drag at 0° AoA, and the normal force is a little more than 2 times the axial force. At the first level of verification and validation, the functions that are obtained by integrating over the surface of the DARPA SUBOFF are compared, and the agreement is good.

4.3 Pressure and wall shear stress

The pressure and wall shear stress are studied at the second level of verification. In Fig. 6, $\emptyset$ is measured in the clockwise direction from the y axis. In the BRM, the body is rotated anticlockwise to simulate AoA, whereas in the FRM, the flow is rotated anticlockwise – as shown in Fig. 6. Therefore, $\emptyset = 0°$ is the windward side in the BRM and the leeward side in the FRM. In the FRM (half body) method, $z = 0$ is the symmetry plane and $\emptyset = 0°$ and 180° are on this plane.

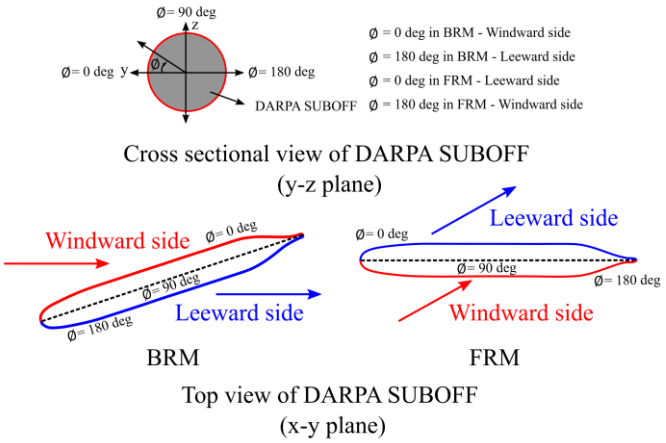

Fig. 6: The description of the azimuthal angle, windward and leeward side on DARPA SUBOFF in FRM and BRM method during angle of attack.

The distributions of pressure computed using BRM 360° and FRM 180° models at α = 18.11° are shown in Fig. 7 at $z = 0$ (*x*-*y* plane in top view). The stagnation point is the point at which the inward normal to the convex nose region is along the flow direction, and the pressure is maximum here. The maximum pressure is 5586.30 Pa and 5585.95 Pa for the BRM 360° and FRM 180° methods, respectively. The difference is about 0.0063%. The minimum pressures are -3628.33 Pa and -3872.80 Pa, and the difference is about 6.3%. Therefore, both methods

yield very nearly the same maximum and minimum pressure, though the FRM 180° the model has 22.84% less cells than the BRM 360° model.

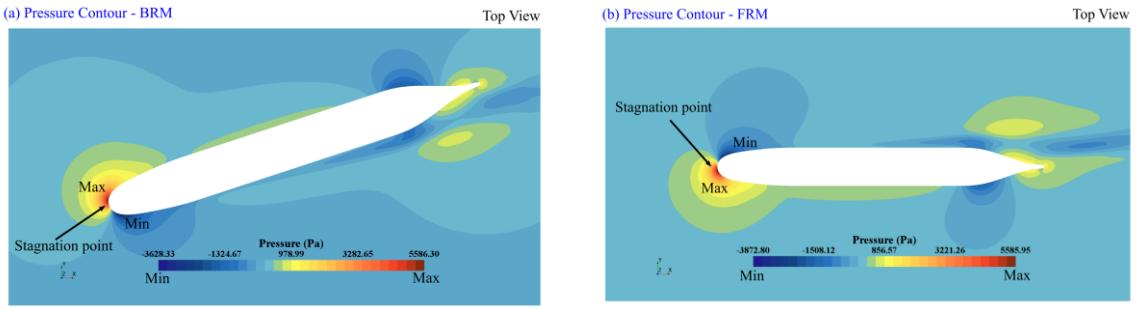

Fig. 7: Pressure contour at α =18.11° (a) BRM 360° (b) FRM 180°

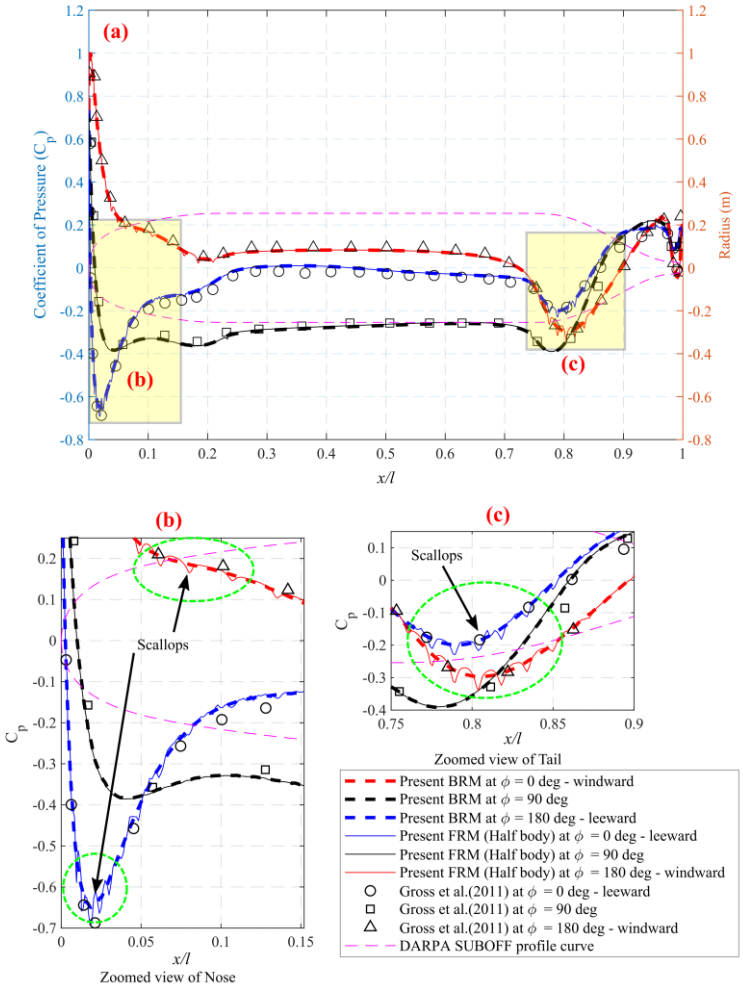

Fig. 8: (a) Coefficient of Pressure at α = 18.11° and ∅ = 0°, 90° and 180° computed in the present study using BRM 360° and FRM 180° models and by Gross et al. (2011) (b) zoom of the nose region (c) zoom of tail region.

The coefficient of pressure, $C_p = (P - P_{ref})/(0.5\rho u_{ref}^2)$, where P_{ref} is the reference pressure or ambient pressure equal to 0 Pa, P is the static pressure in Pa, $\rho = 999.1026$ kg/m^3 is the density of water and $u_{ref} =$ 3.344 m/s is the reference velocity as it corresponds to Re = 12.5× 10^6. The C_p obtained by using the BRM

360° and FRM 180° models is shown in Fig. 8a at ∅ = 0°, 90°, and 180°. It is compared with numerical results from Gross et al. (2011) at $Re = 14\times 10^6$, and there is good agreement for all the cases. The maximum value of C_p at the stagnation point is 0.99, and the minimum value of C_p is -0.69. Only the pressure computed using the FRM (half body) model has scallops. They occur at ∅ = 0 and 180° which lie on the symmetry plane. The scallops are clearly seen in the zooms of the nose and tail shown in Fig. 8b and 8c, respectively. They occur at $0 < x/l < 0.15$ in the nose region and $0.75 < x/l < 0.9$ in the tail region even though the mesh in the region in the neighborhood of the symmetry plane is refined. They are not present in the mid-body region, where the surface mesh is coarser (9 mm) than in the nose and tail regions (6 mm) because the field variables vary slowly here.

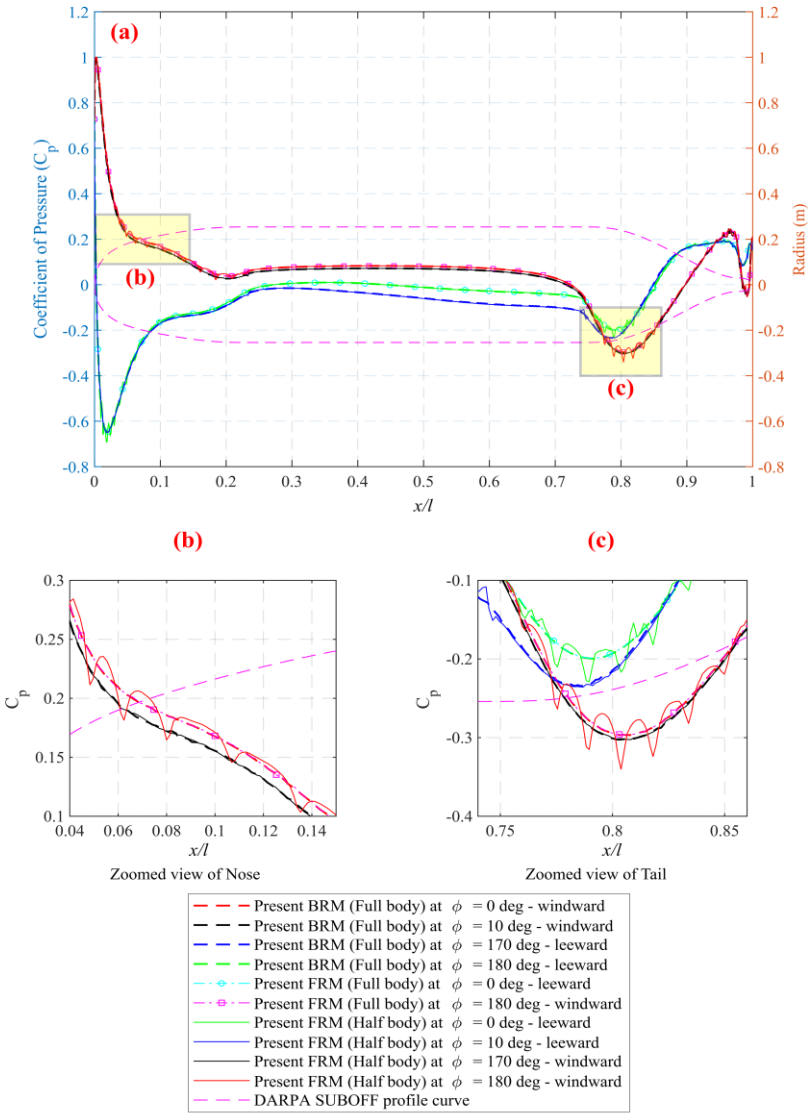

Fig. 9: (a) Coefficient of Pressure at α =18.11° and ∅ = 0°, 10°, 170°, and 180° computed in the present study using BRM 360°, FRM 360° and FRM 180° models. (b) zoom of the nose region (c) zoom of the tail region.

The distance between consecutive peaks and troughs in the scallops is non-uniform. The FRM 180° model has only 45% less cells than in the FRM 360° model as the mesh near the symmetry plane is refined. The disadvantage is the presence of the scallops. It is seen from Fig. 8 that the scallops are not present in the interior of the meshed volume. To show this C_p at $\emptyset = 0°, 10°, 170°$, and 180° are shown in Fig. 9a and the zoomed views of the nose and tail regions are shown in Fig. 9b and 9c.

In our previous work (Krishna et al., 2023), numerical simulations were done using 2D axisymmetric and 3D simulations at $\alpha = 0°$. The results show that adverse pressure gradient $(\partial P/\partial x) > 0$ exists in the regions $0.85 < x/l < 1.0$. But in the present study, the regions vary with $\emptyset$, as seen in Fig. 8 and 9. $(\partial P/\partial x)$ is greater than 0 at $0.0 < x/l < 0.72$, $0.9 < x/l < 0.985$, and $0.996 < x/l < 1.0$ on the windward side, $0 < x/l < 0.01$, and $0.86 < x/l < 1.0$ at $\emptyset = 90°$, and $0 < x/l < 0.003$, $0.28 < x/l < 0.44$, and $0.85 < x/l < 1.0$ on the leeward side. The largest value of $(\partial P/\partial x)$ occurs at the nose on the windward side.

The coefficient of wall shear stress (C_τ) is computed using $C_\tau = \tau_w/(0.5\rho u_{ref}^2)$ where, τ_w is the wall shear stress (N/m^2). The contour map of wall shear stress on the surface of DARPA SUBOFF for BRM 360° and FRM 180° models at α =18.11° is shown in Fig. 10 and provides a big picture. In this figure, the minimum value is less than 1% of the maximum value. There are large patches where it is very low on the leeward side. The maximum obtained using the FRM 180° model is about 15% more than that obtained using the BRM 360° model.

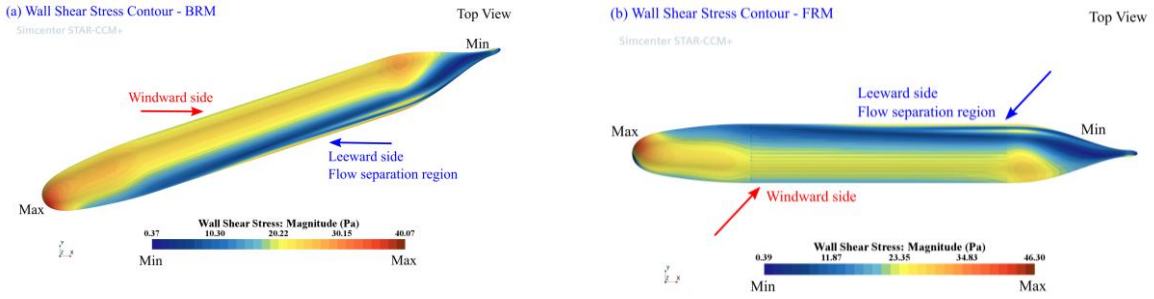

Fig. 10: Wall shear stress contour for DARPA SUBOFF in BRM and FRM at α =18.11 °

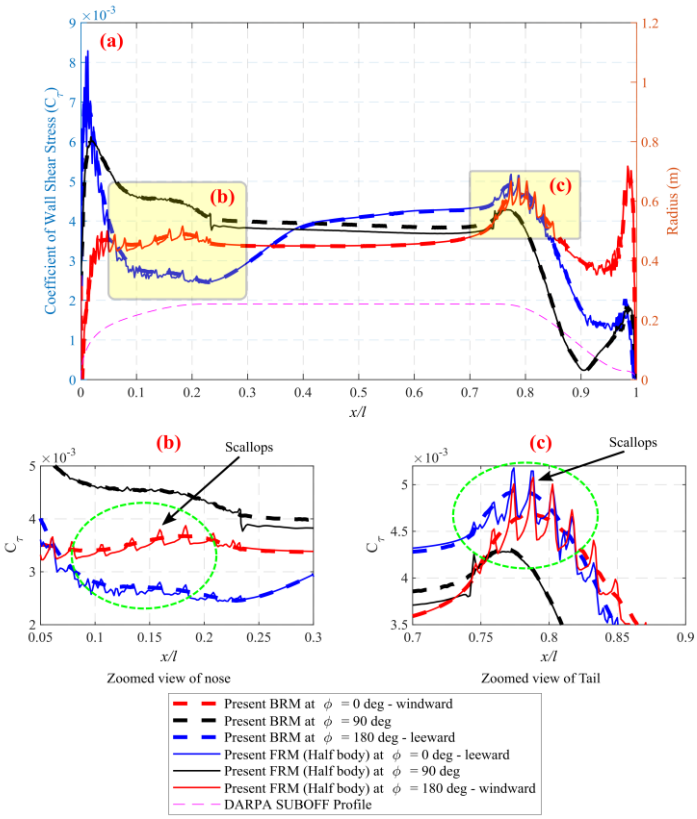

Fig. 11: (a) Coefficient of Wall Shear Stress at α = 18.11° and $\emptyset$ = 0°, 90° and 180° computed in the present study using BRM and FRM (b) zoom of the nose region (c) zoom of tail region.

The details of C_τ distribution at various x/l locations are shown in Fig. 11 at $\emptyset$ = 0°, 90°, and 180°. The stress obtained using the FRM 180° model has scallops on the symmetry plane at 0.05 < x/l < 0.3 (nose) and at 0.7 < x/l < 0.9 (tail). The zoomed views of scallops in the nose and tail regions are shown in Fig. 11b and 11c, respectively.

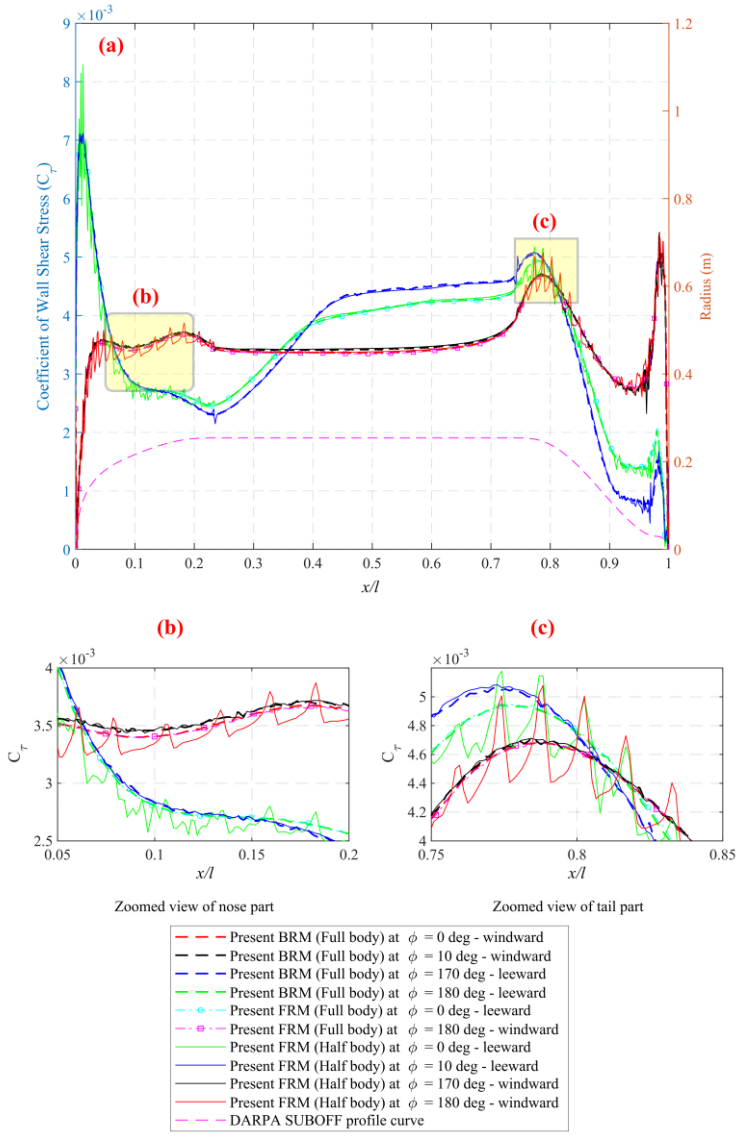

Fig. 12: (a) Coefficient of Wall Shear Stress at α = 18.11° and $\emptyset$ = 0°, 10°, 170°, and 180° computed in the present study using BRM and FRM. (b) zoom of the nose region (c) zoom of the tail region.

No scallops are present in the C_τ curve for BRM, and $\emptyset = 90°$ in FRM. At $\emptyset = 90°$, in the FRM 180° model results, there is a small discontinuity in the stress where the parallel mid-body begins and where it ends. It is again concluded that the use of the symmetry plane leads to scallops in functions that are evaluated on the symmetry plane. As scallops are seen on the symmetry plane, the wall shear stress is investigated near it. The stress computed at $\emptyset$ = 0°, 10°, 170°, 180° is shown in Fig. 12. The stresses found using the 360° models are nearly the same on the windward side as well as on the leeward side. However, when the FRM 180° model is used, there are large scallops on the leeward side of the symmetry plane where the stress is high near the nose. Therefore, it is not good to use the 180° model if the local stress is of interest. Scallops can occur due to a symmetry plane, improper mesh refinement, or poor geometric tessellation density. In the present study, care was taken to make mesh refinements

and tessellation density very fine. Hence, these parameters did not affect scallops. The main reasons for scallops in the present study were due to the use of a symmetry plane.

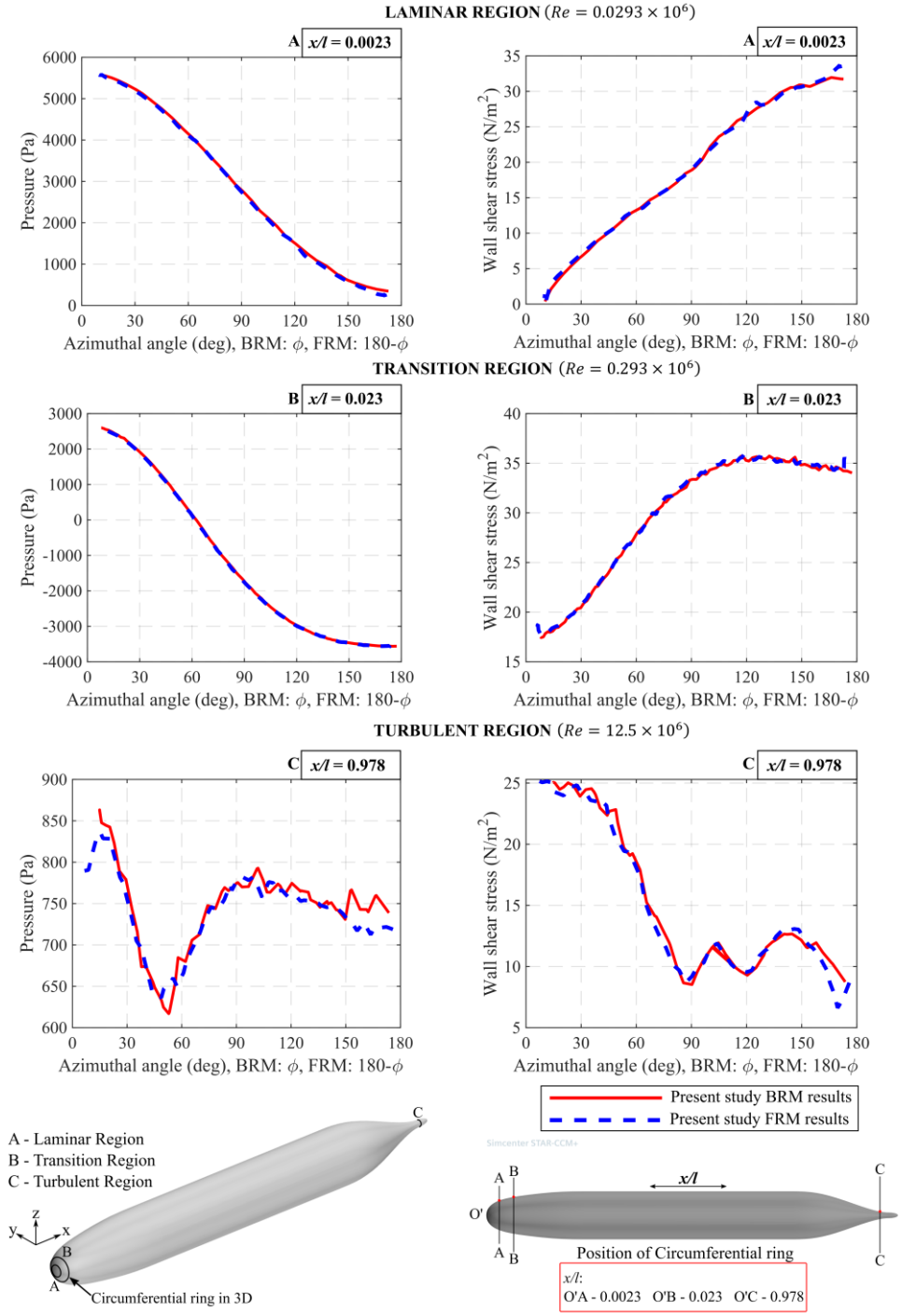

Fig. 13: Circumferential distribution of pressure and wall shear stress at various locations from the leading edge of DARPA SUBOFF at α =18.11°. Azimuthal angle is Ø in BRM and 180-Ø in FRM.

At the second level of verification, the distributions of pressure and wall shear stress in the circumferential direction are also studied. In Fig. 13, they are shown at various distances from the leading edge of the nose. These distances are chosen based on local *Re* such that they are in the laminar, transition, and turbulent flow regimes. In STAR-CCM+, a circumferential ring is created as a derived part that circumscribes the surface of the DARPA SUBOFF. For the BRM 360° model, Ø = 0° is on the windward side and Ø = 180° is on the leeward side. For the

FRM model, $\emptyset = 0°$ is on the leeward side and $\emptyset = 180°$ is on the windward side. To compare the pressure and wall shear stress, the FRM results at $\emptyset = 180°$ to $0°$ are plotted on top of the BRM results at $\emptyset = 0$ to $180°$. The values shown on the x-axis are for the BRM results.

At $x/l = 0.0023$ and 0.023, the Reynolds number based on distance from the nose is 0.0293 and 0.293 million, respectively. Therefore, the flow could be laminar and in transition, respectively. At $x/l = 0.978$, Re is 12.5 million, and the flow is turbulent. At $x/l = 0.0023$ and 0.023, the pressure keeps dropping as $\emptyset$ increases. At $x/l = 0.0023$, the wall shear stress also keeps dropping. The pressure at $x/l = 0.978$ and the wall shear stress at $x/l = 0.023$ and 0.978 have both positive and negative slopes. However, all the results obtained using the BRM and FRM are in good agreement. Thus, the second verification level between FRM and BRM is also completed.

4.4 Velocity distribution

At the third level of verification, the velocity distributions around the DARPA SUBOFF were computed using the BRM 360° and FRM 180° models at $\alpha = 18.11°$ and results are shown in Fig. 14a and 14b. The maximum velocity value estimated using FRM is 4.270 m/s, whereas it is 4.304 m/s when BRM is used. The relative difference is 0.80%. Streamlines using BRM and FRM are shown in Fig. 14c and 14d. They start on the z = 0 plane but go over the DARPA SUBOFF. Streamlines that go over the tail start out forward of amidships. Huang and Liu (1994) present experimental results for non-dimensional axial and radial velocity profiles at various stern locations of DARPA SUBOFF at $\alpha = 0°$. They are also computed using 2D axisymmetric and 3D simulations in Krishna et al. (2023). However, experimentally determined velocity profiles at $\alpha = 18.11°$could not be found in the literature.

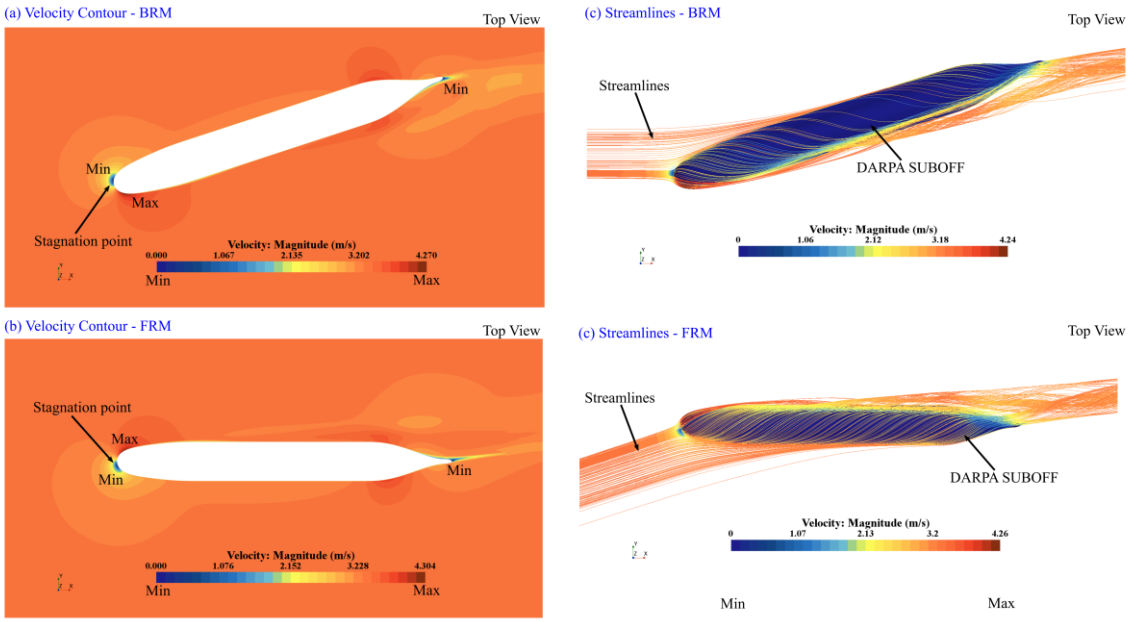

Fig. 14: Velocity contours and streamlines around bare hull DARPA SUBOFF at $\alpha = 18.11°$. (a) and (c) are computed using BRM, and (b) and (d) are computed using FRM.

The axial velocity profiles, computed using the BRM 360° and FRM 180° models, at various stern locations of the DARPA SUBOFF, at $\alpha = 18.11°$, are shown in Fig. 15 on the windward and leeward sides. All line probes used for computing the velocity profiles lie on the $z = 0$ plane. The results are in fair agreement, and the differences are visible. The non-dimensional velocity profiles computed using the BRM 360° and FRM 180° models at the tail where $x/l = 0.978$ are shown in Fig. 16. In the figure, $Y^+ = y_p \frac{u_\tau}{v}$ and $U^+ = u_x/u_\tau$, where u_x is the axial velocity and u_τ is the frictional velocity. The profiles are shown on the $z = 0$ plane and are similar to velocity profiles for flat plate flow. The agreement is good at $Y^+ < 10$ and fair at higher values. On the windward side, the velocity reaches a maximum value and then plateaus out at $Y^+ > 500$. On the leeward side, the disturbance

due to the body is seen at large distances from the body. The BRM 360° and FRM 180° model results are similar, but a small difference is seen in the figure.

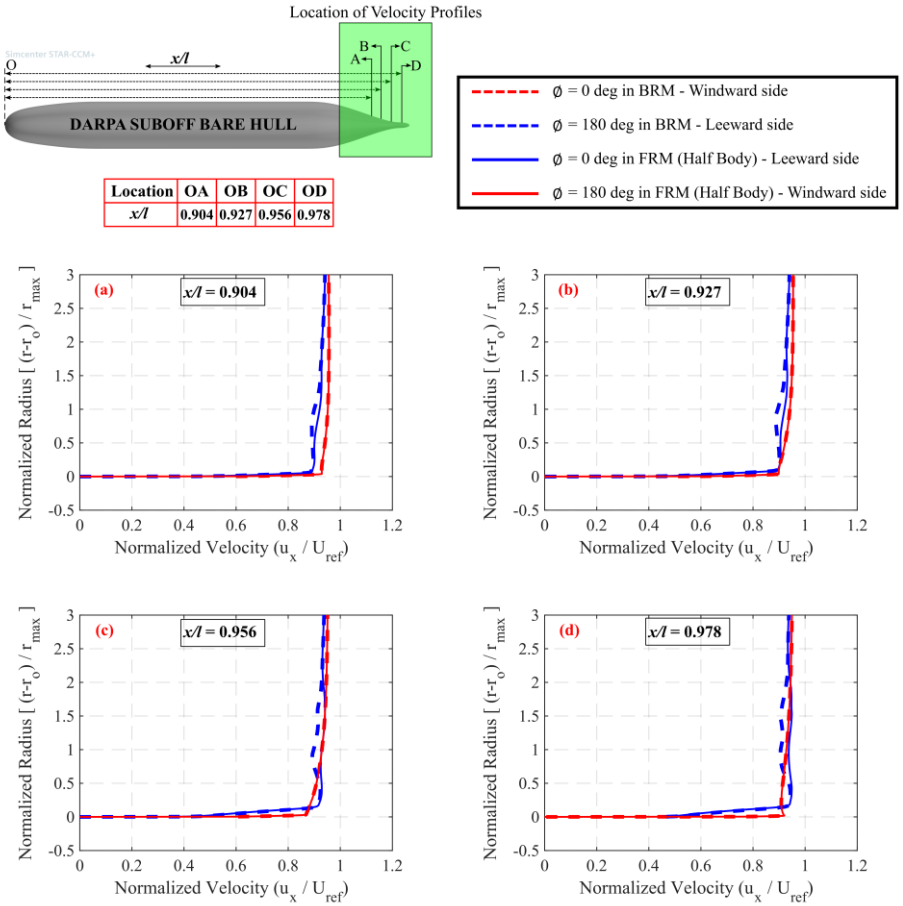

Fig. 15: Normalized axial velocity profiles estimated using BRM and FRM at various locations from the leading edge of DARPA SUBOFF in windward and leeward sides at α = 18.11°.

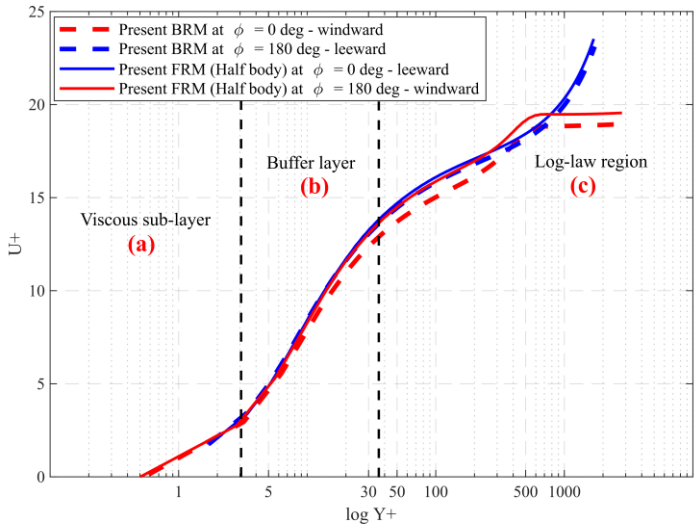

Fig. 16: Normalized velocity profile (U+ vs Y+) plot at x/l = 0.978 at α = 18.11°.

4.5 Overview of comparison between FRM and BRM

An overview of the BRM 360°, FRM 180°, and FRM 360° model results are shown in Table 4. The relative error between BRM and FRM results in estimating the coefficients of hydrodynamic forces and moments is less than 2%, whereas for estimating primary flow variables like pressure and velocity fields, the relative error is less than 1%. The results estimated using BRM 360° is found to be much closer to FRM 360° than FRM 180° models.

Table 4: Comparison of BRM and FRM results at α =18.11°

Parameter	BRM	FRM	FRM
Body of Revolution(degrees)	360° (Full body)	180° (Half body)	360° (Full body)
Axial force coefficient (X')	7.164×10^{-4}	7.178×10^{-4}	7.178×10^{-4}
Normal force coefficient (Y')	5.954×10^{-3}	6.033×10^{-3}	5.964×10^{-3}
Moment coefficient (M')	3.358×10^{-3}	3.342×10^{-3}	3.357×10^{-3}
Drag (N)	256.73	259.38	257.21
Lift (N)	551.29	558.92	552.25
Computation Time for 6,500 steps (hrs.)	49	41	83
No of cells in mesh (Million – M)	24.43	18.85	34.51
Avg Y_w^+	0.38	0.42	0.38
Stagnation Pressure (Pa)	5586.30	5589.45	5584.09
Max. velocity (m/s)	4.27	4.30	4.27

The overall computation time required for FRM 360° is 69% more than what is required for BRM 360° model. The reason for this huge computational time is mainly due to the occupancy of 41% more cells in the FRM 360° model compared to BRM (reason for increase in cell count for FRM 360° model discussed in the previous section 2). Also, using an FRM 180° model with a symmetry plane reduces the computational time by a factor of 16% only from BRM, but at the cost of the presence of visible scallops in pressure and wall shear stress plots, which is not acceptable when near-wall physics is of interest. Hence, the best option to simulate angle of attack studies will be BRM 360° method in terms of the accuracy of results and saving computational resources and time.

5. Conclusions

A detailed comparison is presented for the results obtained using the BRM 360°, FRM 180°, and FRM 360° methods for angle of attack studies for the DARPA SUBOFF submarine model. The details of the mesh, computation time, and quantitative results are presented and used to draw broad conclusions regarding the advantages and disadvantages of the BRM and FRM methods. BRM 360° and FRM 360° give nearly the same results, but the FRM 180° method yields results on the symmetry plane with scallops. The BRM 360° models require significantly fewer cells than the FRM 360° models. Though it requires a little more user time to generate a mesh for each angle of attack, the iteration or solution time is less. Therefore, it is concluded that the BRM 360° method is the best.

Verification and validation are given prime importance. Comparison of the BRM and FRM results is itself a form of verification. The hydrodynamic forces and moments that are obtained by integrating over the surface of the DARPA SUBOFF are at the first level. Richardson extrapolation is used to determine the relative error, order of accuracy, and grid convergence index when the mesh size tends to zero. The pressure and wall shear stress distribution on the surface is at the second level. Velocity profiles and their fields are at the third level of verification. The differences between the results obtained using the BRM 360° and FRM 360° methods are small and unlikely to be significant for practical applications. The $k-\omega$ SST turbulence model is used, and a majority of the wall-adjacent cells have $Y_w^+ < 1$. All the computations are done using several million cells.

The computed hydrodynamic forces and moments results are validated by comparing them with experimental results from DTRC. The present study results are also compared with BRM results from other CFD literature and shown to be in fair agreement. All the details of the mesh are provided and can be reproduced by those with interest. At the highest AoA, α = 18.11°, the difference between the axial, normal, and moment coefficients

computed using the BRM 360°, FRM 360°, and FRM 180° models is less than 2%. The pressure, wall shear stress, and velocity fields, velocity profiles, and streamlines at windward and leeward sides are also presented, which are rarely seen in any recent literature.

The differences between these functions of interest computed using the BRM 360° and FRM 180° are small but not negligible. The FRM 180° model is appealing at first sight, but the results suggest that its use is not advisable. Symmetry planes are used to model only a fraction of the full 360° in several publications and there are recommendations for what the fraction should be. Here, it is shown that even if the mesh in the neighbourhood of the symmetry plane is refined, functions such as the pressure and wall shear stress evaluated on the symmetry plane have scallops, and this inference has not been previously reported in any other literature. These will affect the computed forces and moments. Further, the refinement leads to extra cells, and the total number of cells is 55% of the full 360° model for the same mesh sizes and settings. Therefore, the use of symmetry planes is to be avoided and, if computational resources permit, a full 360° models should be used.

The present study focuses on comparing the BRM and FRM methods for a bare hull submarine model without any fins or appendages. One of the major factors that might cause a difference between BRM and FRM results will be the presence of the control surfaces or rudders on these underwater vehicles. To address this, future work will extend the study by including numerical oblique test simulations on the appended DARPA SUBOFF submarine model at various angles of attack using BRM and FRM methods.

Acknowledgements

All authors of the present study are grateful to all teaching and non-teaching staff and the team members of the Computational Hydrodynamics and Structural Engineering Laboratory (CHASE Lab), Department of Ship Technology, CUSAT, for providing valuable suggestions, guidance, technical support, and computational resources to carry out this research work successfully.

References

Celik, I. B., Ghia, U., Roache, P. J., and Freitas, C. J. (2008). Procedure for estimation and reporting of uncertainty due to discretization in CFD applications. Journal of fluids Engineering-Transactions of the ASME, 130(7). https://doi.org/10.1115/1.2960953

de Barros, E. A., Dantas, J. L., Pascoal, A. M., and De Sá, E. (2009). Investigation of normal force and moment coefficients for an AUV at nonlinear angle of attack and sideslip range. IEEE Journal of Oceanic Engineering, 33(4), 538-549. https://doi.org/10.1109/JOE.2008.2004761

Ebrahimnejad, L., Janoyan, K. D., Yadollahi Farsani, H., Valentine, D. T., and Marzocca, P. (2014). Efficient predictions of unsteady viscous flows around bluff bodies by aerodynamic reduced order models. Journal of Offshore Mechanics and Arctic Engineering, 136(1), 011101. https://doi.org/10.1115/1.4025544

Gomatam, S., Vengadesan, S., and Bhattacharyya, S. K. (2012). Numerical simulations of flow past an autonomous underwater vehicle at various drift angles. Journal of Naval Architecture and Marine Engineering, 9(2), 135-152. https://doi.org/10.3329/jname.v9i2.12567

Gross, A., Jagadeesh, C., and Fasel, H. F. (2013). Numerical and experimental investigation of unsteady three-dimensional separation on axisymmetric bodies. International journal of heat and fluid flow, 44, 53-70. https://doi.org/10.1016/j.ijheatfluidflow.2013.04.016

Gross, A., Kremheller, A., and Fasel, H. (2011). Simulation of flow over suboff bare hull model. 49th AIAA aerospace sciences meeting including the new horizons forum and aerospace exposition (p. 290). https://doi.org/10.2514/6.2011-290

Groves, N. C., Huang, T. T., and Chang, M. S. (1989). Geometric characteristics of DARPA (Defense Advanced Research Projects Agency) SUBOFF models (DTRC model numbers 5470 and 5471) (No. DTRCSHD129801).

Huang, T., and Liu, H. L. (1994). Measurements of flows over an axisymmetric body with various appendages in a wind tunnel: the DARPA SUBOFF experimental program.

ITTC (2011) – Recommended Procedures and Guidelines, Fresh Water and Seawater Properties, International Towing Tank Conference, 7.5-02-01-03.

ITTC (2014) – Recommended Procedures and Guidelines, Practical Guidelines for Ship CFD Applications, International Towing Tank Conference, 7.5-03-02-03.

ITTC (2021) – Recommended Procedures and Guidelines, Uncertainty Analysis in CFD Verification and Validation Methodology and Procedures, International Towing Tank Conference, 7.5-03-01-01.

Krishna, H. R., Issac, M. T., and Ebenezer, D. D. (2023). Numerical investigation of two-dimensional axisymmetric and three-dimensional flow simulations over a benchmark underwater vehicle. Physics of Fluids, 35(1). https://doi.org/10.1063/5.0134985

Kumar, K. H., Koppula, S. B., Alamanda, S. S., and Vemireddi, S. (2023). Aerodynamic study of flow past autonomous underwater vehicle at varying angles of attack. International Conference on Smart Materials and Structures, ICSMS-2022 (Vol. 2810, No. 1, p. 140005). AIP Publishing LLC. https://doi.org/10.1063/5.0146890

Le, T. L., and Hong, D. T. (2021). Computational fluid dynamics study of the hydrodynamic characteristics of a torpedo-shaped underwater glider. Fluids, 6(7), 252. https://doi.org/10.3390/fluids6070252

Leong, Z. Q., Ranmuthugala, D., Penesis, I., and Nguyen, H. D. (2015). RANS-based CFD prediction of the hydrodynamic coefficients of DARPA SUBOFF geometry in straight-line and rotating arm manoeuvres. International Journal of Maritime Engineering, 157(A1). https://doi.org/10.5750/ijme.v157iA1.947

Lin, J., Wang, S., Yao, H. D., and Su, Y. (2024). Angle of attack impact on flow characteristics around finite-length rotating columns. Physics of Fluids, 36(6). https://doi.org/10.1063/5.0209233

Liu, H. L., and Huang, T. T. (1998). Summary of DARPA SUBOFF experimental program data (No. CRDKNSWCHD129811).

Madan, A. D., and Issac, M. T. (2017). Hydrodynamic analysis of AUV hulls using semi-empirical and CFD approach. Univers. J. Mech. Eng, 5(5), 137-143. https://doi.org/10.13189/ujme.2017.050501

Mohamed, A., Kchaou, H., Mohamed, A., and Driss, Z. (2017). Numerical Study of Attack's Angle Effect on Drag Coefficient of AUV Hull Design. American Journal of Mechanical Engineering, 5(1), 8-13.

Praveen, P. C., and Krishnankutty, P. (2013). Study on the effect of body length on the hydrodynamic performance of an axi-symmetric underwater vehicle. Indian Journal of Geo-Marine Sciences, 42(8), 1013-1022.

Ray, A. (2010). Analysis of manoeuvring hydrodynamics of underwater vehicles. (Doctoral dissertation, Indian Institute of Technology Madras).

Ray, A., Singh, S. N., and Seshadri, V. (2009, January). Evaluation of linear and nonlinear hydrodynamic coefficients of underwater vehicles using CFD. International Conference on Offshore Mechanics and Arctic Engineering (Vol. 43444, pp. 257-265). https://doi.org/10.1115/OMAE2009-79374

Ray, S., Chatterjee, D., and Nandy, S. (2016). unsteady cfd simulation of 3D AUV hull at different angles of attack. Journal of Naval Architecture and Marine Engineering, 13(2), 111-123. https://doi.org/10.1115/OMAE2009-79374

Roddy, R. F. (1990). Investigation of the stability and control characteristics of several configurations of the DARPA SUBOFF model (DTRC Model 5470) from captive-model experiments (No. DTRCSHD129808).

Sakthivel, R., Vengadesan, S., and Bhattacharyya, S. K. (2011). Application of non-linear k-ε turbulence model in flow simulation over underwater axisymmetric hull at higher angle of attack. Journal of Naval Architecture and Marine Engineering, 8(2), 149-163. https://doi.org/10.3329/jname.v8i2.6984

Shereena, S. G., Vengadesan, S., Idichandy, V. G., and Bhattacharyya, S. K. (2013). CFD study of drag reduction in axisymmetric underwater vehicles using air jets. Engineering Applications of Computational Fluid Mechanics, 7(2), 193-209. https://doi.org/10.1080/19942060.2013.11015464

Subburaj, R., Khandelwal, P., and Vengadesan, S. (2018). Numerical study of flow past an elliptic cylinder near a free surface. Physics of Fluids, 30(10). https://doi.org/10.1063/1.5046745

Takahashi, K., and Sahoo, P. K. (2019, June). Fundamental CFD study on the hydrodynamic performance of the DARPA SUBOFF submarine. International Conference on Offshore Mechanics and Arctic Engineering (Vol. 58776, p. V002T08A052). American Society of Mechanical Engineers. https://doi.org/10.1115/OMAE2019-96190